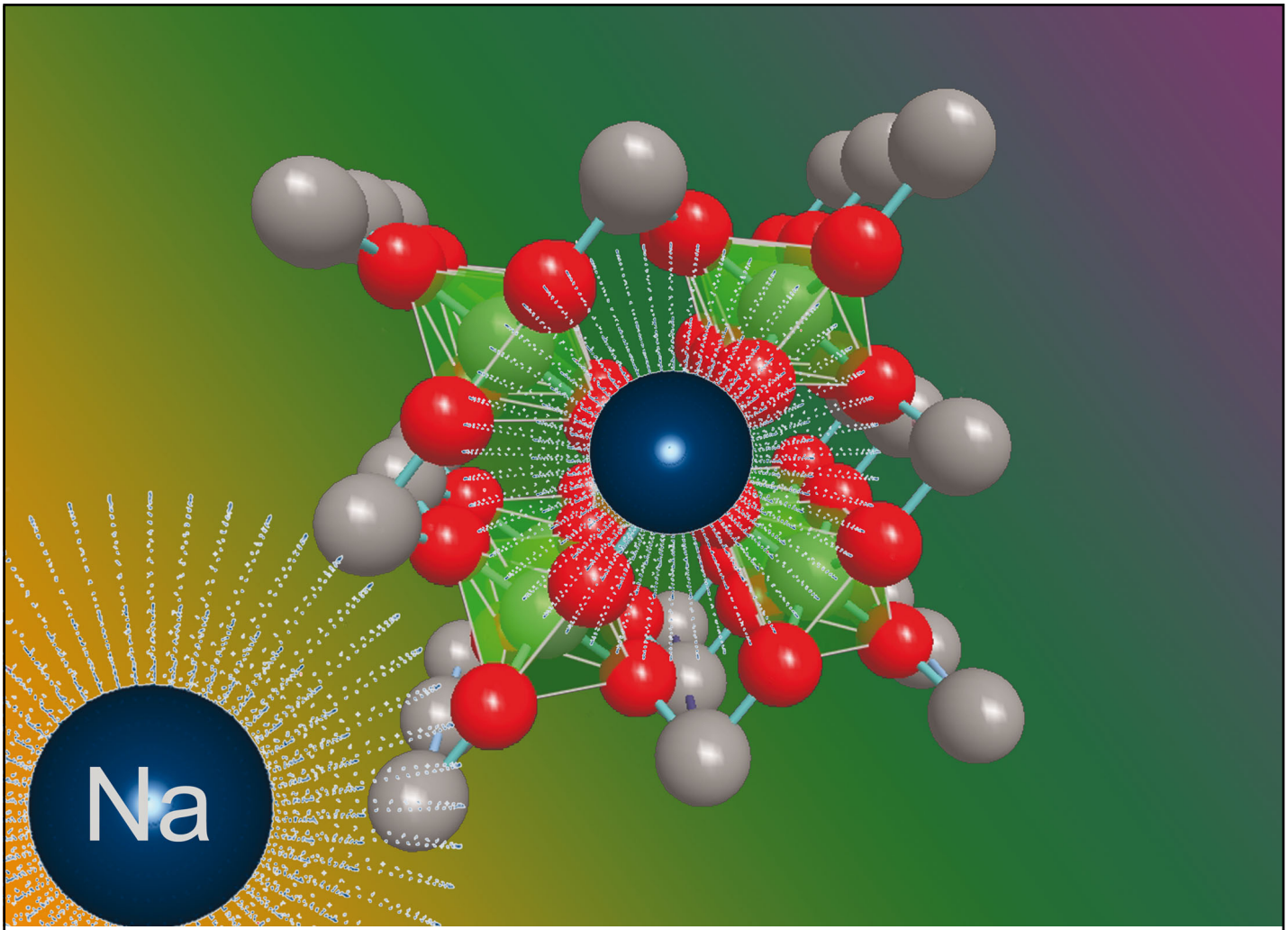

Showcasing collaborations between the Centre for Clean Energy Technology at the University of Technology, Sydney, Australia and WCU Centre for Next Generation Batteries at Gyeongsang National University, South Korea

Title: Octahedral tin dioxide nanocrystals as high capacity anode materials for Na-ion batteries

This work introduces the synthesis of octahedral SnO_2 single crystals with dominantly exposed {221} active facets as anode materials for sodium-ion batteries. The exposed (1×1) tunnel-structure could facilitate the initial insertion of Na ions. The mechanism of the reversible Na storage in SnO_2 crystals was revealed by *ex situ* TEM analyses.

As featured in:

See Wang *et al.*, *Phys. Chem. Chem. Phys.*, 2013, **15**, 12543.

www.rsc.org/pccp

Registered Charity Number 207890

PCCP

RSC Publishing

PAPER

View Article Online
View Journal | View Issue

Cite this: *Phys. Chem. Chem. Phys.*, 2013, **15**, 12543

Octahedral tin dioxide nanocrystals as high capacity anode materials for Na-ion batteries†

Dawei Su,[a] Chengyin Wang,[b] Hyojun Ahn[c] and Guoxiu Wang*[a]

Received 14th May 2013,
Accepted 29th May 2013

DOI: 10.1039/c3cp52037d

www.rsc.org/pccp

Single crystalline SnO_2 nanocrystals (~60 nm in size) with a uniform octahedral shape were synthesised using a hydrothermal method. Their phase and morphology were characterized by XRD and FESEM observation. TEM and HRTEM analyses identified that SnO_2 octahedral nanocrystals grow along the [001] direction, consisting of dominantly exposed {221} high energy facets. When applied as anode materials for Na-ion batteries, SnO_2 nanocrystals exhibited high reversible sodium storage capacity and excellent cyclability (432 mA h g^{-1} after 100 cycles). In particular, SnO_2 nanocrystals also demonstrated a good high rate performance. *Ex situ* TEM analysis revealed the reaction mechanism of SnO_2 nanocrystals for reversible Na ion storage. It was found that Na ions first insert into SnO_2 crystals at the high voltage plateau (from 3 V to ~0.8 V), and that the exposed (1 × 1) tunnel-structure could facilitate the initial insertion of Na ions. Subsequently, Na ions react with SnO_2 to form Na_xSn alloys and Na_2O in the low voltage range (from ~0.8 V to 0.01 V). The superior cyclability of SnO_2 nanocrystals could be mainly ascribed to the reversible Na–Sn alloying and de-alloying reactions. Furthermore, the reduced Na_2O ''matrix'' may help retard the aggregation of tin nanocrystals, leading to an enhanced electrochemical performance.

1. Introduction

Sodium-ion batteries have recently attracted great interest owing to their low cost and the natural abundance of sodium. The sodium intercalation chemistry is very similar to Li, and its voltage, stability and diffusion barriers are competitive with Li-ion systems.[1] Much progress on Na-ion batteries has been achieved. For cathode materials, layered transition metal oxides such as P_2-Na_xCoO_2,[2,3] P_2-$Na_{2/3}[Fe_{1/2}Mn_{1/2}]O_2$,[4] $Na_{2/3}(Ni_{1/3}Fe_{1/3}Mn_{2/3})O_2$,[5] $NaCrO_2$,[6,7] Na_xMnO_2,[8,9] Na_xVO_2,[10] $Na_3V_2(PO_4)_3$,[11,12] with stable capacities were reported. Furthermore, olivine $NaFePO_4$,[13] fluoride-based materials, $NaMF_3$ (M = Fe, Mn, V and Ni),[14,15] fluorophosphate[16] and fluorosulfate[17–19] have also been developed. For anode materials, most studies focused on hard carbon materials due to their large interlayer distance and disordered structure, which facilitates Na-ion insertion–extraction.[20–22] However, Dahn *et al.* reported that the Na-intercalated hard carbon (Na_xC) has higher reactivity with the non-aqueous electrolyte than Li_xC_6, raising new concerns about the stability of the electrolyte.[23] Alternative oxide anodes such as $Na_2Ti_3O_7$,[24] $Li_4Ti_5O_{12}$,[25] $Na_2C_8H_4O_4$,[26] and amorphous TiO_2-nanotubes[27] have also been investigated. All of them showed less than 300 mA h g^{-1} capacities. Transition metal oxides have been extensively investigated as high capacity anodes for Li-ion batteries.[28–32] Therefore, it could be possible to apply transition metal oxides for Na ion storage in Na-ion batteries. However, none of them demonstrated comparable performances for Na-ion batteries.

Recently, it was reported that SnSb/C nanocomposites based on Na alloying reactions exhibited a good performance as anodes for Na-ion batteries.[33] Similarly, SnO_2 can be reduced by Na, generating Sn and further alloying with Na. Therefore, SnO_2 could potentially be used as an anode material for Na-ion storage. Herein, we provide the first report on SnO_2 nanocrystals with exposed {221} high energy facets as anode materials for Na-ion batteries, which exhibited a high reversible capacity and an excellent cycling performance. The reaction mechanism has been identified using *ex situ* TEM analyses.

[a] *Centre for Clean Energy Technology, School of Chemistry and Forensic Science, Faculty of Science, University of Technology, Sydney, Australia. E-mail: Guoxiu.Wang@uts.edu.au; Fax: +61 2 9514 1460; Tel: +61 2 9514 1741*
[b] *College of Chemistry and Chemical Engineering, Yangzhou University, 180 Si-Wang-Ting Road, Yangzhou 225002, China*
[c] *School of Materials Science and Engineering, Gyeongsang National University, Jinju, Gyeongnam 660-701, Republic of Korea*

† Electronic supplementary information (ESI) available: Low magnification FESEM, TEM images, and geometric models of as-prepared octahedral SnO_2. Crystal structure of octahedral SnO_2 viewed from [110] and [001] directions, the profile of octahedral SnO_2 being initially discharged to 0.8 V. *d*-Spacing & Miller indices of different crystals of SnO_2, Sn, Na_9Sn_4, and Na_2O. See DOI: 10.1039/c3cp52037d

2. Methods

2.1. Synthesis of SnO_2 nanocrystals

SnO_2 nanocrystals were synthesized using a hydrothermal method. In a typical synthesis process, 2 mmol $SnCl_2{\cdot}5H_2O$ (Sigma-Aldrich, $\geq$98%) was dissolved in 10 mL deionized water. Then 0.315 g polyvinyl pyrrolidone (PVP) as a surfactant was added. After stirring for at least 30 minutes, 0.4 mL H_2SO_4 (2M) was added into the precursor solution. After stirring for several more minutes, it was heated to 200 °C in a Teflon-lined autoclave (25 mL in capacity) for 12 h. The precipitate was cooled to room temperature naturally, then collected and washed with distilled water and ethanol several times. After drying at 60 °C in a vacuum oven overnight, the final products were obtained.

2.2. Structural and physical characterization

The phases of SnO_2 nanocrystals were characterized by X-ray diffraction (XRD, Siemens D5000) using Cu Kα radiation at a scanning step of 0.02° s^{-1}. The morphology was observed using a field emission scanning electron microscope (FESEM, Zeiss Supra 55VP). The crystal structures were analysed using transmission electron microscopy (TEM) and high-resolution transmission electron microscopy (HRTEM, JEOL JEM-2011). Fast-Fourier-Transform (FFT) patterns were recorded using a Gatan CCD camera in a digital format.

2.3. Electrochemical testing

The testing electrodes were prepared by dispersing SnO_2 nanocrystals (70 wt%), acetylene carbon black (20 wt%), and poly(vinylidene fluoride) binder (PVDF, 10 wt%) in *N*-methyl-2-pyrrolidone (NMP) to form a slurry. The resultant slurry was pasted onto copper foil and dried in a vacuum oven for 12 h, followed by pressing at 200 kg cm^{-2}. Electrochemical measurements were carried out using two-electrode coin cells with Na foil as counter and reference electrodes and a glass microfibre (Whatman) as the separator. The CR2032-type coin cells were assembled in an argon-filled glove box (UniLab, Mbraun, Germany). The electrolyte solution was 1 M $NaClO_4$ dissolved in a mixture of ethylene carbonate (EC) and propylene carbonate (PC) with a volume ratio of 1 : 1. The charge–discharge measurements were performed at ambient temperature at different current densities in the voltage range from 0.01 to 3 V. In order to investigate the sodium-driven structural and morphological changes of SnO_2 nanocrystals, Swagelok-type cells were assembled. After the first discharge and 100 cycles, the cells were disassembled and soaked in PC in a glove-box for 24 h to remove the organic residues before being used for *ex situ* TEM analysis.

3. Results and discussion

3.1. Morphology and crystal structure

The phase of SnO_2 nanocrystals was identified by XRD (Fig. 1) and refined by the Rietveld method[34] (as implemented by the GSAS software suite) between 10° and 90°. All diffraction peaks can be indexed to the SnO_2 phase with a space group of $P4_2/mnm$, having a tetragonal symmetry unit cell with satisfactory convergence factors

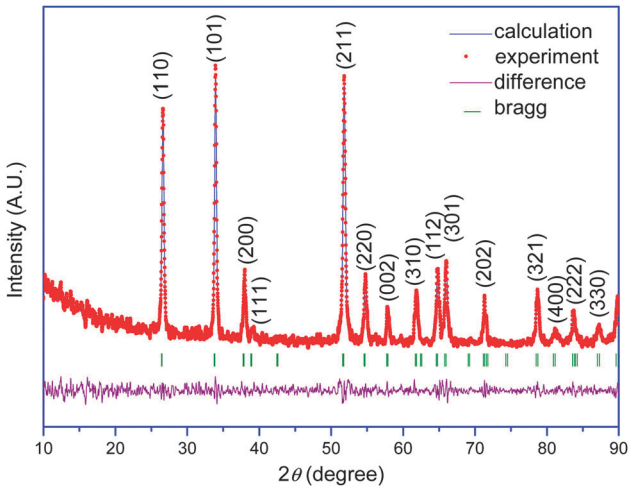

Fig. 1 Rietveld refinement pattern and XRD data of SnO_2 nanocrystals. The observed and calculated results are represented by red dots and blue solid line, respectively. The bottom wine-coloured line shows the fitting residual difference. Bragg positions are represented by light-green ticks.

(χ^2 = 3.7, R_{wp} = 6.33%, R_p = 4.72%). No impurity phases were present. The morphology of SnO_2 nanocrystals was observed by FESEM (as shown in Fig. 2). The sample consists of uniform octahedral shape and homogenous size distribution with an average size of less than 60 nm (Fig. 2a). SnO_2 nanocrystals show a well-defined octahedral shape with an edge-to-edge width of about 40 nm, and an apex-to-apex length of around 60 nm (Fig. 2b and c). The geometry model of SnO_2 nanocrystals is illustrated in Fig. 2d.

The detailed crystal structure of SnO_2 nanocrystals was analysed by TEM, HRTEM and FFT. The low magnification TEM image presents the uniform size and shape distribution of SnO_2 nanocrystals (as shown in Fig. S1, ESI†). Fig. 3a, c and e present high magnification TEM images of three free standing SnO_2 nanocrystals, from which we can observe their outlines along different projected directions. Their geometries were simulated and illustrated as insets in Fig. 3a, c and e. Fig. 3b, d and f show the lattice resolved HRTEM images and Fast-Fourier-Transform (FFT) patterns, which were taken from marked rectangular areas in Fig. 3a, c and e, respectively. Fig. 3b was recorded from the apex of the octahedral SnO_2. Its corresponding FFT pattern (inset in Fig. 3b) can be well indexed along the [110] zone axis of the tetragonal SnO_2. The (110) crystal planes are clearly visible, in which the orthogonal (001) and $(1\bar{1}0)$ lattices with 0.31 nm and 0.33 nm *d*-spacings have been identified. Through the HRTEM image (Fig. 3d) and its FFT pattern (inset in Fig. 3d), we can identify that the top view of the SnO_2 nanocrystal is along the [001] zone axis of tetragonal SnO_2, suggesting that octahedral SnO_2 nanocrystals grow along the [001] orientation. When rotating the SnO_2 crystal to a small angle from [110] (Fig. 3e), the orthogonal $(11\bar{1})$ and $(1\bar{1}0)$ lattices with 0.23 nm and 0.33 nm *d*-spacings can be determined (Fig. 3f) and its FFT pattern can be indexed along the [112] zone axis (as shown as the inset in Fig. 3f). Based on the above TEM observations and structural analysis,

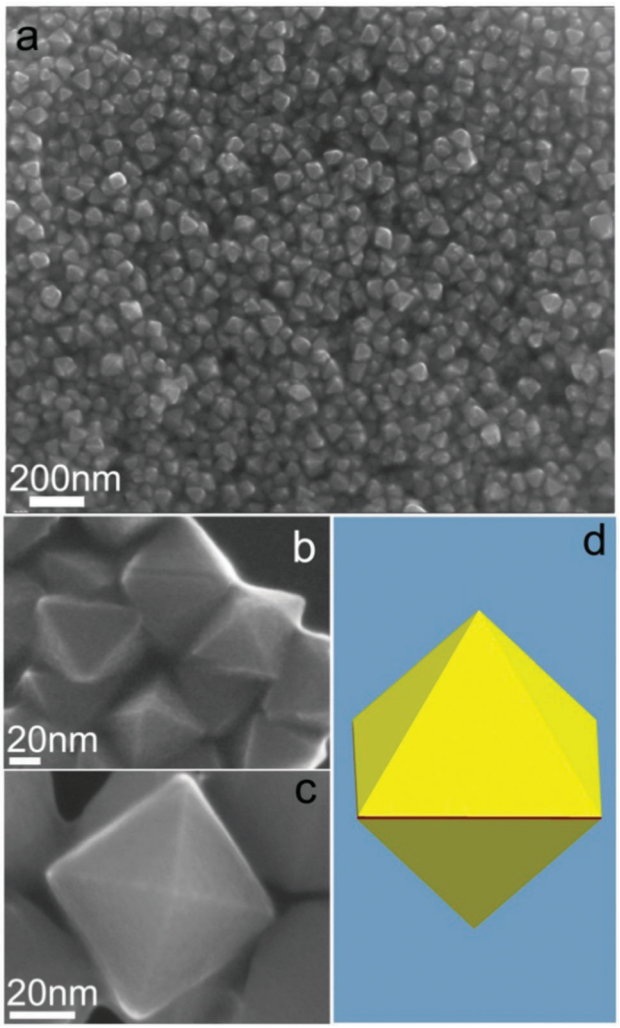

Fig. 2 (a) Low magnification FESEM image of octahedral SnO_2 nanocrystals. (b) and (c) High magnification FESEM images of typical free standing octahedral SnO_2 nanocrystals. (d) The geometric model of octahedral SnO_2 nanocrystals.

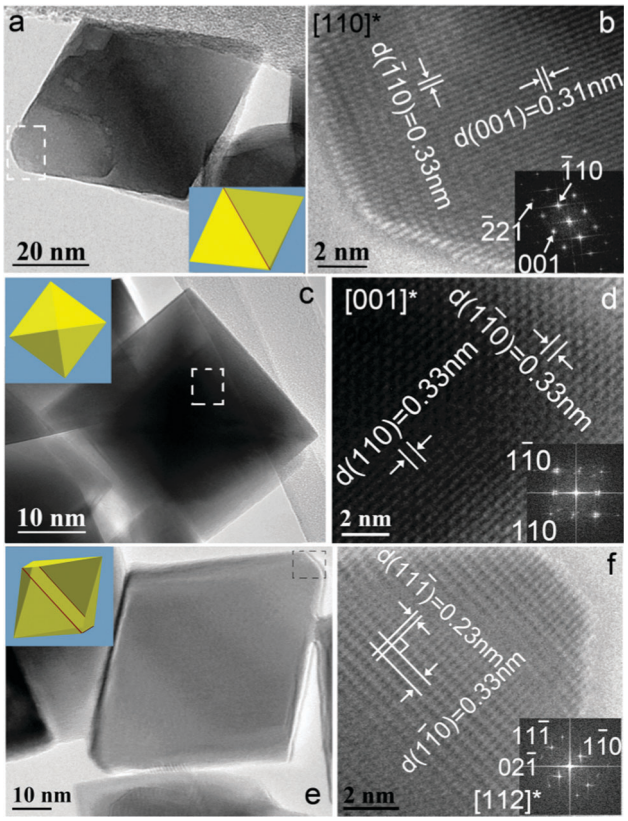

Fig. 3 Typical TEM images of a single octahedral SnO_2 crystal viewed along [110] (a), [001] (c), and [112] (e) directions; (b), (d), and (f) are lattice resolved HRTEM images taken from the marked rectangular area in (a), (c), and (e), respectively. Insets in (a), (c), and (e) are the illustration of their corresponding geometric models viewed along different projected directions. Insets in (b), (d), and (f) are their corresponding Fast-Fourier-Transform (FFT) patterns.

we can conclude that the pyramid planes of the as-prepared octahedral SnO_2 nanocrystals are {221} facets, which are illustrated in Fig. S2–S4 (ESI†).

3.2. Crystal growth mechanism

During the synthesis process, adding an appropriate amount of suitable acid is crucial for the formation of octahedral SnO_2 nanocrystals. It has been reported that perfect octahedral SnO_2 nanocrystals exposed with {221} facets can only be obtained within a narrow window of acidity by adding HCl.[35] The suitable acid H_2SO_4 used in this research successfully controlled SnO_2 crystal size and suppressed the growth of crystals. As a result, SnO_2 nanocrystals with almost 100% exposed {221} facets were obtained. The {221} facets of SnO_2 have a relatively higher surface energy (2.28 J m^{-2}) than other low-index facets such as {110} (1.401 J m^{-2}), {101} (1.554 J m^{-2}), and {100} (1.648 J m^{-2}) facets.[36] It is well known that high-energy surfaces usually exhibit unique physical and chemical properties. For example, TiO_2 crystals with 46% high energy {001} facets demonstrated excellent photocatalytic activity.[37] It was also reported that TiO_2 with dominantly exposed {001} facets exhibited high performance as anode materials in Li-ion batteries.[38,39] A Co_3O_4 nanomesh with exposed {112} crystal planes demonstrated high capacitance as an electrode material for supercapacitors.[40] Therefore, we expect that SnO_2 nanocrystals with exposed high-energy {221} facets could provide reactive sites for reaction with sodium ions (at least in the initial reduction process, which is critical for subsequent cycling),[41] leading to enhanced electrochemical performance for sodium storage in Na-ion batteries.

3.3. Electrochemical properties for sodium storage in Na-ion batteries and discussions on the reaction mechanism

When applied as anodes for Na-ion batteries, octahedral SnO_2 nanocrystals exhibited a superior electrochemical performance for sodium ion storage. Fig. 4 shows the discharge and charge curves of SnO_2 nanocrystals. SnO_2 nanocrystals achieved 1773 mA h g^{-1} discharge capacity in the initial cycle, which is higher than the theoretical sodium storage capacity of SnO_2 due to the decomposition of the electrolyte,[42] then dropped to 540 mA h g^{-1} in the second cycle. The discharge capacity stabilised at the level of more than 500 mA h g^{-1} in the subsequent cycles. These values are comparable with the previous reported anode

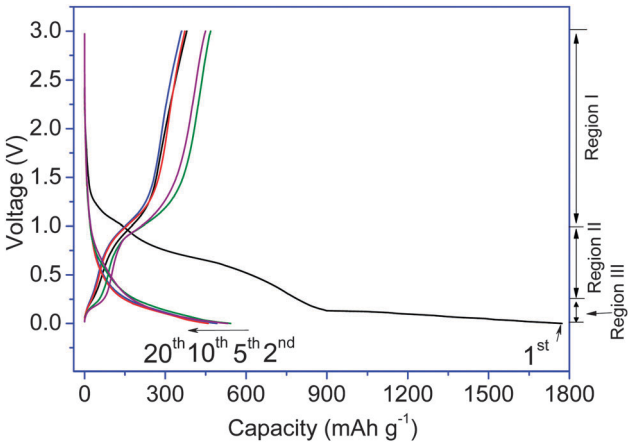

Fig. 4 Discharge and charge profiles of octahedral SnO_2 nanocrystals in the 1st, 2nd, 5th, 10th, and 20th cycles.

materials for Na-ion batteries.[20–22,33] From the second cycle, the discharge and charge curves are well overlapped, indicating the high reversibility and good capacity retention of the electrode. The initial low Coulombic efficiency could be ascribed to the formation of a solid electrolyte interface (SEI) layer in the first cycle. The finding of new electrolytes and additives could overcome this problem. From the first discharge profile, we can clearly observe three slope regions: I. 3.0 V–0.8 V, II. 0.8 V–0.1 V, and III. 0.1 V–0.01 V. According to the previous reports,[43–46] and *in situ* X-ray diffraction studies on the SnO_2 applied in Li-ion batteries,[47] lithium ions first react with SnO_2 to form an amorphous Li_2O matrix and Sn, followed by Sn alloying with Li to form Li_xSn. Herein, we propose three steps in the first discharge process. The region I corresponds to the Na ion insertion into SnO_2 nanocrystals:

$$Na^+ + SnO_2 \rightarrow NaSnO_2 \quad (1)$$

The region II can be assigned to the reduction of SnO_2 nanocrystals:

$$SnO_2 + 4Na^+ + 4e^- \rightarrow Sn + 2Na_2O \quad (2)$$

while region III is ascribed to the Na–Sn alloying reaction and the formation of a solid-electrolyte interface (SEI).[47,48]

$$Sn + xNa^+ + xe^- \rightarrow Na_xSn \quad (3)$$

For anodic curves, all cycles present two well-defined slope regions: from 0.01 V to 0.5 V and from 0.5 V to 1.3 V. The former indicates the de-alloying reaction of Na_xSn. While the latter corresponds to the reversible reaction between Sn and Na_2O to re-generate SnO_2. On the other hand, we should pay attention to the slope region I in this first discharge curve, which disappeared from the second cycle. We propose that the region I corresponds to the Na ion insertion into the SnO_2 crystal structure along the [001] direction. The tetragonal SnO_2 crystal has a (1×1) channel structure composed of individual chains of SnO_6 octahedral units, which are feasible for Na ion insertion because the radius of the Na ion (1.02 Å) is smaller than the (1×1) tunnel size (2.3 Å × 2.3 Å) (as illustrated in Fig. S5, ESI†).

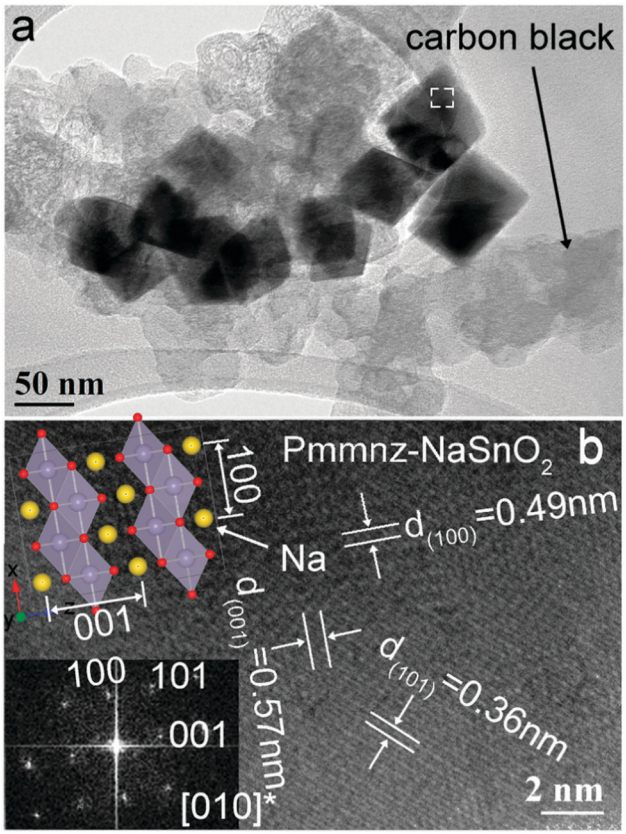

Fig. 5 *Ex situ* TEM images of octahedral SnO_2 nanocrystals after discharged to 0.8 V. (a) is the low magnification TEM image. (b) Lattice resolved HRTEM image taken from the rectangle area marked in (a). The bottom inset in (b) is the corresponding FFT pattern, which can be well indexed along the [010] zone axis of *Pmmnz*-$NaSnO_2$. The top inset in (b) is the crystal structure of *Pmmnz*-$NaSnO_2$ along the [010] projected direction.

When we discharged the cells to 0.8 V, we found that the obtained capacity corresponds to 1 mol Na inserting into 1 unit mol SnO_2 and generating $NaSnO_2$ (Fig. S6, ESI†).

This presumption was confirmed by *ex situ* TEM analysis on the electrode after discharged to 0.8 V (as shown in Fig. 5). It can be seen that the shape of SnO_2 nanocrystals was preserved without any degradation of the crystallinity (Fig. 5a and b), suggesting Na ion insertion into the SnO_2 crystal structure at the high voltage plateau (above 0.8 V). This phenomenon has also been observed in the high voltage range for transition metal oxide anode materials in Li-ion batteries.[49] From the lattice resolved HRTEM image (Fig. 5b, taken from the marked rectangle area in Fig. 5a) and its corresponding FFT (the bottom inset in Fig. 5b) patterns, we identified that the generated $NaSnO_2$ nanocrystals have the orthorhombic symmetry with the *Pmmnz* space group. The $NaSnO_2$ crystal structure was further confirmed by the (001), (101) and (100) crystal planes with *d*-spacings of 0.57 nm, 0.36 nm and 0.49 nm, respectively.

In order to verify the proposed mechanism in region II, we discharged the SnO_2 electrode to 0.1 V and performed the *ex situ* TEM analysis (Fig. 6). As shown in Fig. 6a, the octahedral morphology of SnO_2 nanocrystals has changed due to further

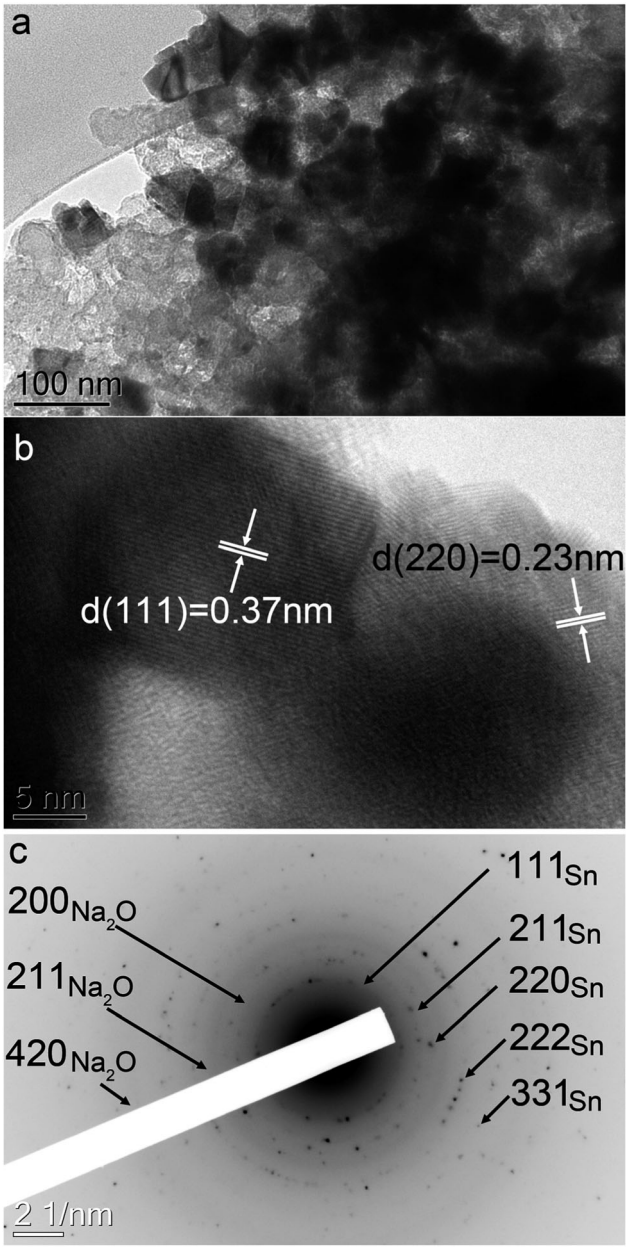

Fig. 6 *Ex situ* TEM images of octahedral SnO_2 nanocrystals after discharged to 0.1 V. (a) Is the low magnification TEM image. (b) Is the lattice resolved HRTEM image. (c) Is the corresponding SAED pattern, showing the presence of Na_2O and Sn.

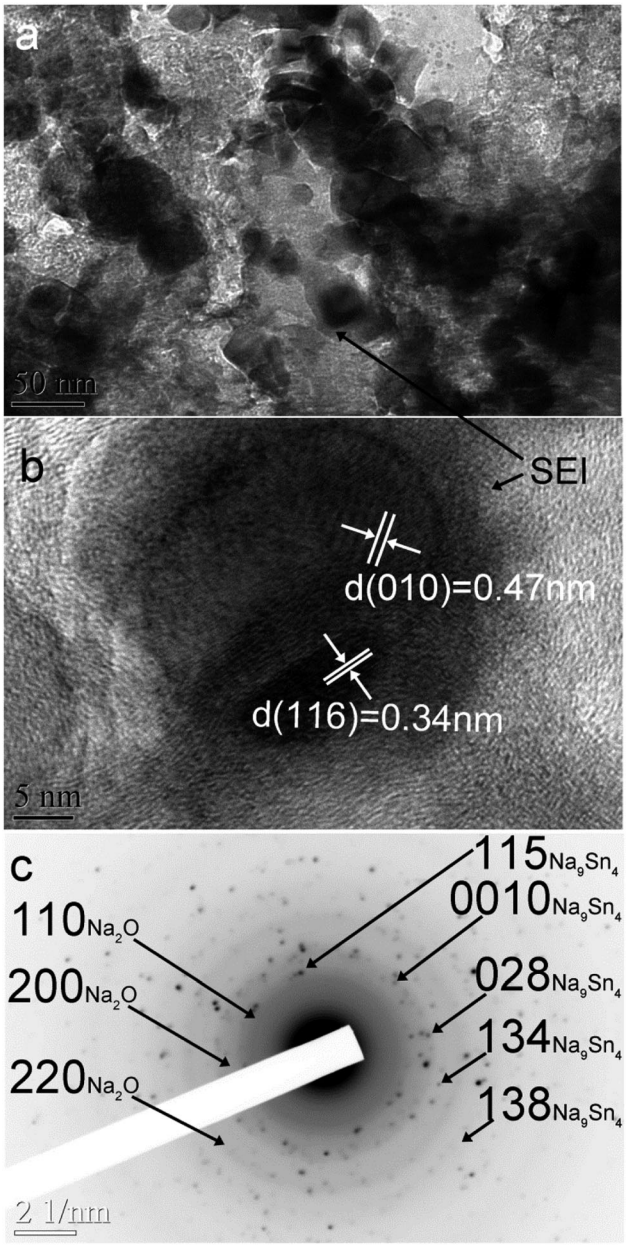

Fig. 7 *Ex situ* TEM images of octahedral SnO_2 nanocrystals after discharged to 0.01 V. (a) Is the low magnification TEM image. (b) Is the lattice resolved HRTEM image. (c) Is the SAED pattern taken from the marked area in (b), showing the presence of Na_2O and Na_9Sn_4.

reaction with sodium. The lattice resolved HRTEM image is shown in Fig. 6b, in which the lattice spacings of the Sn(111) and Sn(220) crystal planes were determined to be 0.37 nm and 0.23 nm, respectively. Fig. 6c shows the corresponding SAED pattern. The diffraction rings can be indexed to Sn and Na_2O. The *ex situ* TEM analysis clearly proved the formation of Sn and Na_2O in region II.

When the SnO_2 electrode was discharged to 0.01 V, the *ex situ* TEM images presented different features. As shown in Fig. 6, SnO_2 nanocrystals lost their shape and morphology. We observed tiny nanocrystals embedded in the amorphous matrix (as shown in Fig. 7a). The HRTEM image (Fig. 7b) further revealed the pseudo-amorphous characteristic, suggesting the formation of the solid electrolyte interface layer (SEI) on the surface of individual crystals. The corresponding SAED pattern proved the existence of the Na_9Sn_4 ($Na_{2.25}Sn$) alloy (Fig. 7c, *d*-spacing & Miller indices of SnO_2, Sn, Na_2O and Na_9Sn_4 are shown in Table S1, ESI†). This unambiguously confirmed the alloying formation in the low voltage range. Moreover, the SAED pattern also shows the (110), (200) and (220) weak diffraction rings of Na_2O, which suggests the formation of a Na_2O matrix surrounding the Na_xSn nanocrystals.

Based on the above *ex situ* TEM analysis, the initial discharge process of SnO_2 nanocrystals in Na-ion cells could

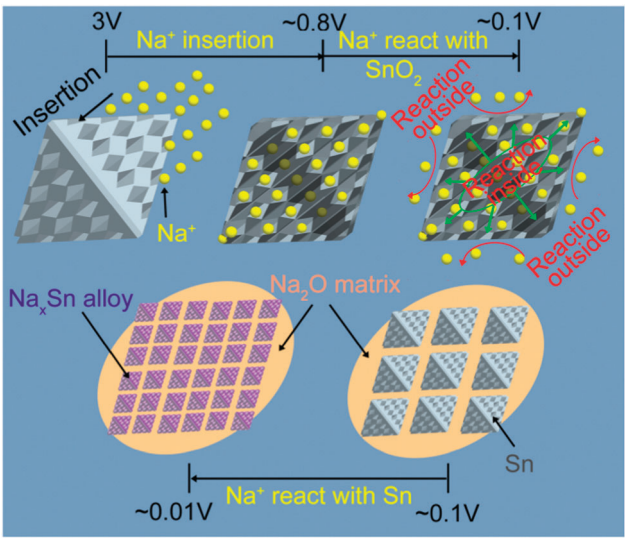

Fig. 8 The schematic illustration of the mechanism for the initial discharge process of SnO_2 nanocrystals as an anode in the Na-ion battery. At the high voltage plateau (from 3 V to ~0.8 V), Na ions insert into SnO_2 nanocrystals. Subsequently, in the low voltage range (from ~0.8 V to 0.01 V), two step reactions between SnO_2 and Na proceed not only from the surface, but also from the inside of SnO_2 nanocrystals.

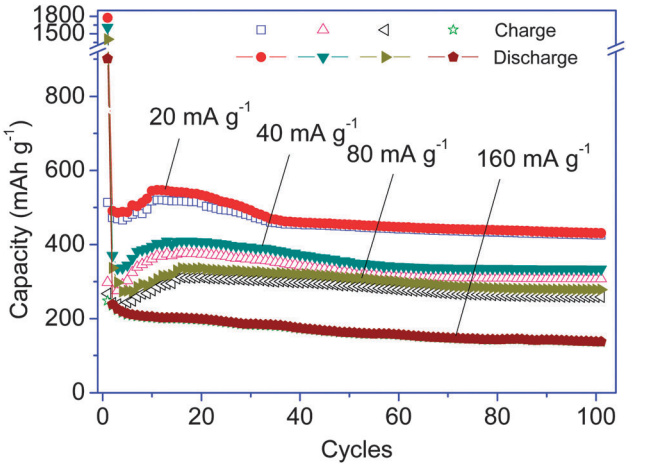

Fig. 9 Charge and discharge capacities *vs.* cycle number of octahedral SnO_2 nanocrystals at current densities of 20, 40, 80 and 160 mA g^{-1}.

be ascribed to two different mechanisms. As illustrated in Fig. 8, Na ion insertion occurs at the high voltage plateau (from 3 V to ~0.8 V), during which the compact (1 × 1) tunnel-structure along the [001] direction of tetragonal SnO_2 could facilitate the insertion of Na. Subsequently, in the low voltage range (from ~0.8 V to 0.01 V), two step reactions between SnO_2 and Na proceed as: $SnO_2 + 4Na \rightarrow 2Na_2O + Sn$ and $9Na + 4Sn \rightarrow Na_9Sn_4$.

In particular, the initial discharge process is crucial for the performance of the electrode in the following cycles. The inserted Na ions in the initial high voltage range can facilitate the conversion reaction between SnO_2 and Na to proceed not only from the outside surface, but also from the inside of the SnO_2 crystals. The as-prepared octahedral SnO_2 nanocrystals grow along the [001] direction, which are exposed with the (1 × 1) tunnels as illustrated in Fig. S5 (ESI†). Therefore, Na ions can facilely insert into the crystal structure of SnO_2 crystals. On the other hand, the as-prepared octahedral SnO_2 nanocrystals are exposed with high-energy {221} facets. They could provide reactive sites for the reaction with sodium ions, leading to the enhanced electrochemical performance for sodium storage in Na-ion batteries. Furthermore, the formed Na_2O matrix could also retard the aggregation of Sn and Na_xSn alloy particles, resulting in reversible alloying and de-alloying reaction between Sn and Na.

The long-term cycling performances (up to 100 cycles) of octahedral SnO_2 nanocrystals were tested at different current densities and the results are shown in Fig. 9, demonstrating the superior capacity retention and high rate capability. The electrochemical performance is much better than the nano-metre-sized SnO_2 (less than 20 nm, as shown in Fig. S7–S9 in ESI†). The rate performances of as-prepared octahedral SnO_2 nanocrystals are also superior to those of previously reported

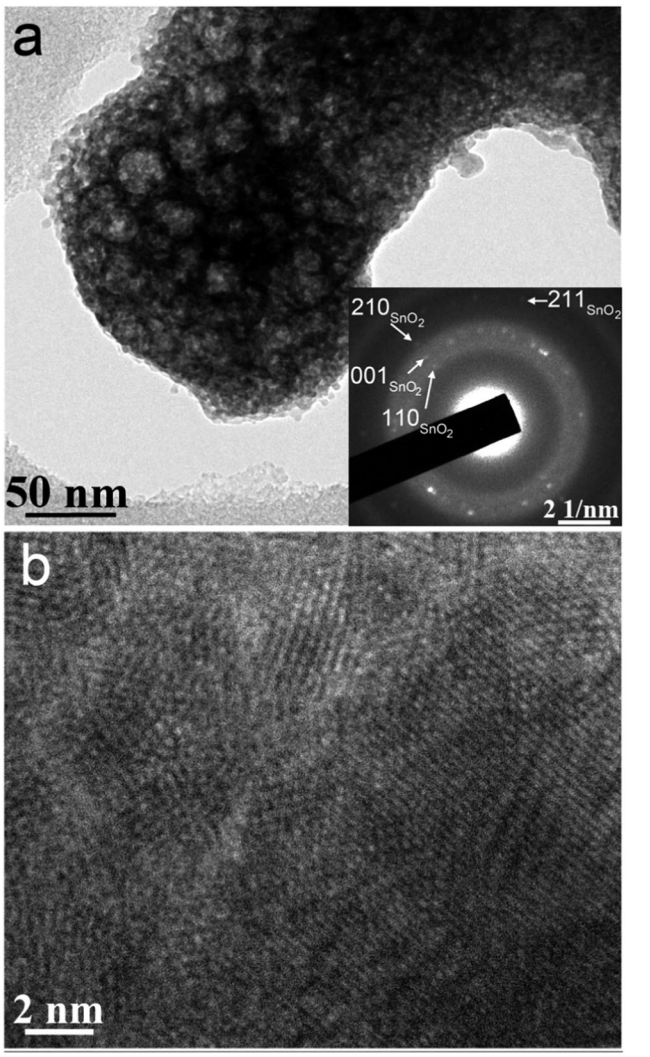

Fig. 10 *Ex situ* TEM analysis of the SnO_2 nanocrystal electrode after 100 cycles. (a) Low magnification TEM image of the electrode at the full charge state. The inset is the SAED pattern. (b) Lattice resolved HRTEM image of SnO_2 nanocrystals at the full charge state.

hard carbon materials,[20–22] and alternative oxide anodes such as $Na_2Ti_3O_7$ (ref. 24) and TiO_2-nanotubes.[27]

The cycled SnO_2 nanocrystal electrode was examined using *ex situ* TEM analysis (Fig. 10). At the fully charged state after 100 cycles, SnO_2 nanocrystals have lost their octahedral shape and completely disintegrated into less than 4 nm nanoparticles (Fig. 10a and b). The SnO_2 nanocrystals did not aggregate into large clusters, which should benefit the reversible alloying and de-alloying process, inducing excellent capacity retention.[44] This is because large particles cannot endure volume changes during discharge and charge processes, leading to cracking and crumbling of the electrode and capacity loss.[46] The well distributed SnO_2 nanoparticles might be ascribed to the Na_2O matrix, which can retard the aggregation of tin into large coherent clusters. The SAED pattern (shown as the inset in Fig. 10a) can be indexed to the SnO_2 phase, which verifies the full reversal back to SnO_2 at the charge state even after 100 cycles. This clearly confirmed the reversible sodium storage in SnO_2 nanocrystal electrodes.

4. Conclusions

Octahedral SnO_2 ($\sim$60 nm) nanocrystals were synthesised using a simple hydrothermal method. The uniform nanocrystals are fully enclosed by {221} facets and grow along the [001] direction, which were identified by TEM and HRTEM analyses. When applied as anode materials for Na-ion batteries, SnO_2 nanocrystals demonstrated a high sodium storage capacity and an excellent cycling performance. Based on the results of *ex situ* TEM analysis, we proposed that Na ions can easily insert into the exposed (1×1) tunnel structures in SnO_2 nanocrystals along the [001] direction in the high voltage range during the initial discharge process (from 3 V to 0.8 V), inducing the full reaction between Na and SnO_2. The exposed high energy {221} facets also provide reactive sites for the reaction with sodium ions, leading to enhanced electrochemical performance for sodium storage in Na-ion batteries. The *ex situ* TEM analysis also revealed that SnO_2 nanocrystals can be fully reversed back to the original phase after 100 cycles.

Acknowledgements

This research is financially supported by the Australian Research Council through the ARC Discovery project (DP1093855) and Future fellowship project (FT110100800). We also acknowledge the support from the National Research Foundation of Korea through the World Class University (WCU) program (R32-2008-000-20093-0).

Notes and references

1 S. P. Ong, V. L. Chevrier, G. Hautier, A. Jain, C. Moore, S. Kim, X. H. Ma and G. Ceder, *Energy Environ. Sci.*, 2011, **4**, 3680–3688.
2 R. Berthelot, D. Carlier and C. Delmas, *Nat. Mater*, 2011, **10**, 74–80.
3 M. M. Doeff, Y. P. Ma, M. Y. Peng, S. J. Visco, L. C. Dejonghe, *Energy Environment Economics: 28th Intersociety Energy Conversion Engineering Conference (Iecec-93)*, 1993, vol. 1, pp. 1111–1116.
4 N. Yabuuchi, M. Kajiyama, J. Iwatate, H. Nishikawa, S. Hitomi, R. Okuyama, R. Usui, Y. Yamada and S. Komaba, *Nat. Mater.*, 2012, **11**, 512–517.
5 D. Kim, E. Lee, M. Slater, W. Q. Lu, S. Rood and C. S. Johnson, *Electrochem. Commun.*, 2012, **18**, 66–69.
6 S. Komaba, C. Takei, T. Nakayama, A. Ogata and N. Yabuuchi, *Electrochem. Commun.*, 2010, **12**, 355–358.
7 X. Xia and J. R. Dahn, *Electrochem. Solid–State Lett.*, 2012, **15**, A1–A4.
8 A. Mendiboure, C. Delmas and P. Hagenmuller, *J. Solid State Chem.*, 1985, **57**, 323–331.
9 R. Stoyanova, D. Carlier, M. Sendova-Vassileva, M. Yoncheva, E. Zhecheva, D. Nihtianova and C. Delmas, *J. Solid State Chem.*, 2010, **183**, 1372–1379.
10 D. Hamani, M. Ati, J.-M. Tarascon and P. Rozier, *Electrochem. Commun.*, 2011, **13**, 938–941.
11 Z. L. Jian, W. Z. Han, X. Lu, H. X. Yang, Y.-S. Hu, J. Zhou, Z. B. Zhou, J. Q. Li, W. Chen, D. F. Chen and L. Q. Chen, *Adv. Energy Mater.*, 2013, **3**, 156–160.
12 Z. L. Jian, L. Zhao, H. L. Pan, Y.-S. Hu, H. Li, W. Chen and L. Q. Chen, *Electrochem. Commun.*, 2012, **14**, 86–89.
13 K. Zaghib, J. Trottier, P. Hovington, F. Brochu, A. Guerfi, A. Mauger and C. M. Julien, *J. Power Sources*, 2011, **196**, 9612–9617.
14 I. D. Gocheva, M. Nishijima, T. Doi, S. Okada, J. Yamaki and T. Nishida, *J. Power Sources*, 2009, **187**, 247–252.
15 Y. Yamada, T. Doi, I. Tanaka, S. Okada and J. Yamaki, *J. Power Sources*, 2011, **196**, 4837–4841.
16 N. Recham, J. N. Chotard, L. Dupont, K. Djellab, M. Armand and J. M. Tarascon, *J. Electrochem. Soc.*, 2009, **156**, A993–A999.
17 M. Ati, L. Dupont, N. Recham, J. N. Chotard, W. T. Walker, C. Davoisne, P. Barpanda, V. Sarou-Kanian, M. Armand and J. M. Tarascon, *Chem. Mater.*, 2010, **22**, 4062–4068.
18 P. Barpanda, J. N. Chotard, N. Recham, C. Delacourt, M. Ati, L. Dupont, M. Armand and J. M. Tarascon, *Inorg. Chem.*, 2010, **49**, 7401–7413.
19 M. Reynaud, P. Barpanda, G. Rousse, J. N. Chotard, B. C. Melot, N. Recham and J. M. Tarascon, *Solid State Sci.*, 2012, **14**, 15–20.
20 R. Alcantara, J. M. Jimenez-Mateos, P. Lavela and J. L. Tirado, *Electrochem. Commun.*, 2001, **3**, 639–642.
21 R. Alcantara, P. Lavela, G. F. Ortiz and J. L. Tirado, *Electrochem. Solid–State Lett.*, 2005, **8**, A222–A225.
22 D. A. Stevens and J. R. Dahn, *J. Electrochem. Soc.*, 2000, **147**, 1271–1273.
23 X. Xia, M. N. Obrovac and J. R. Dahn, *Electrochem. Solid–State Lett.*, 2011, **14**, A130–A133.
24 P. Senguttuvan, G. Rousse, V. Seznec, J.-M. Tarascon and M. Rosa Palacin, *Chem. Mater.*, 2011, **23**, 4109–4111.
25 L. Zhao, J. M. Zhao, Y.-S. Hu, H. Li, Z. B. Zhou, M. Armand and L. Q. Chen, *Adv. Energy Mater.*, 2012, **2**, 962–965.
26 L. Zhao, H. L. Pan, Y.-S. Hu, H. Li and L. Q. Chen, *Chin. Phys. B*, 2012, **21**, 028201.

27 H. Xiong, M. D. Slater, M. Balasubramanian, C. S. Johnson and T. Rajh, *J. Phys. Chem. Lett.*, 2011, **2**, 2560–2565.
28 D. Su, M. Ford and G. Wang, *Sci. Rep.*, 2012, **2**, 924.
29 D. W. Su, H. S. Kim, W. S. Kim and G. X. Wang, *Chem.–Eur. J.*, 2012, **18**, 8224–8229.
30 D. W. Su, H. S. Kim, W. S. Kim and G. X. Wang, *Microporous Mesoporous Mater.*, 2012, **149**, 36–45.
31 D. W. Su, J. Horvat, P. Munroe, H. Ahn, A. R. Ranjbartoreh and G. X. Wang, *Chem.–Eur. J.*, 2012, **18**, 488–497.
32 D. Su, H.-J. Ahn and G. Wang, *J. Power Sources*, DOI: 10.1016/j.jpowsour.2012.11.058.
33 L. F. Xiao, Y. L. Cao, J. Xiao, W. Wang, L. Kovarik, Z. M. Nie and J. Liu, *Chem. Commun.*, 2012, **48**, 3321–3323.
34 H. M. Rietveld, *Z. Kristallogr.*, 2011, **226**, Iv.
35 X. Han, M. Jin, S. Xie, Q. Kuang, Z. Jiang, Y. Jiang, Z. Xie and L. Zheng, *Angew. Chem., Int. Ed.*, 2009, **48**, 9180–9183.
36 B. Slater, C. R. A. Catlow, D. H. Gay, D. E. Williams and V. Dusastre, *J. Phys. Chem. B*, 1999, **103**, 10644–10650.
37 H. G. Yang, C. H. Sun, S. Z. Qiao, J. Zou, G. Liu, S. C. Smith, H. M. Cheng and G. Q. Lu, *Nature*, 2008, **453**, 638–641.
38 J. S. Chen, Y. L. Tan, C. M. Li, Y. L. Cheah, D. Luan, S. Madhavi, F. Y. C. Boey, L. A. Archer and X. W. Lou, *J. Am. Chem. Soc.*, 2010, **132**, 6124–6130.
39 C. H. Sun, X. H. Yang, J. S. Chen, Z. Li, X. W. Lou, C. Z. Li, S. C. Smith, G. Q. Lu and H. G. Yang, *Chem. Commun.*, 2010, **46**, 6129–6131.
40 Y. Wang, H. J. Zhang, J. Wei, C. C. Wong, J. Lin and A. Borgna, *Energy Environ. Sci.*, 2011, **4**, 1845–1854.
41 N.-S. Choi, Y. Yao, Y. Cui and J. Cho, *J. Mater. Chem.*, 2011, **21**, 9825–9840.
42 D. W. Su, H.-J. Ahn and G. X. Wang, *Chem. Commun.*, 2013, **49**, 3131–3133.
43 Y. Idota, T. Kubota, A. Matsufuji, Y. Maekawa and T. Miyasaka, *Science*, 1997, **276**, 1395–1397.
44 M. Winter, J. O. Besenhard, M. E. Spahr and P. Novak, *Adv. Mater.*, 1998, **10**, 725–763.
45 C. Kim, M. Noh, M. Choi, J. Cho and B. Park, *Chem. Mater.*, 2005, **17**, 3297–3301.
46 Y. Chen, Q. Z. Huang, J. Wang, Q. Wang and J. M. Xue, *J. Mater. Chem.*, 2011, **21**, 17448–17453.
47 I. A. Courtney and J. R. Dahn, *J. Electrochem. Soc.*, 1997, **144**, 2045–2052.
48 R. Q. Liu, N. Li, D. Y. Li, G. F. Xia, Y. M. Zhu, S. Y. Yu and C. Wang, *Mater. Lett.*, 2012, **73**, 1–3.
49 J. Cabana, L. Monconduit, D. Larcher and M. Rosa Palacin, *Adv. Mater.*, 2010, **22**, E170–E192.

